One-neutron transfer, complete fusion, and incomplete fusion from the ^{9}Be + ^{197}Au reaction

F. Gollan,[1,2] D. Abriola,[1] A. Arazi,[1,2] M. A. Cardona,[1,2] E. de Barbará,[1] J. de Jesús,[1] D. Hojman,[1,2] R. M. Id Betan,[3,4] J. Lubian,[5] A. J. Pacheco,[1,2] B. Paes,[1] D. Schneider,[1] and H. O. Soler[5]

[1]*Laboratorio TANDAR, Comisión Nacional de Energía Atómica, Av. Gral. Paz 1499, BKNA1650 San Martín, Argentina*

[2]*Consejo Nacional de Investigaciones Científicas y Técnicas, Av. Rivadavia 1917, C1033AAJ Buenos Aires, Argentina*

[3]*Instituto de Física Rosario (CONICET-UNR), Esmeralda y Ocampo, S2000EZP Rosario, Argentina*

[4]*Departamento de Física (FCEIA-UNR), Av. Pellegrini 250, S2000BTP Rosario, Argentina*

[5]*Instituto de Física, Universidade Federal Fluminense, Avenida Litorânea s/n, Gragoatá, Niterói, Rio de Janeiro 24210-340, Brazil*

(Received 7 May 2021; accepted 21 July 2021; published 9 August 2021)

In this work, one-neutron transfer (pickup and stripping), complete and incomplete fusion cross sections for the ^{9}Be + ^{197}Au system were measured over a wide range of energies around the Coulomb barrier by the offline γ-ray detection method. Coupled-channel calculations were used to determine the elastic, inelastic, and transfer cross sections. Coupled reaction channel calculations were performed to derive the one-neutron stripping and pickup cross sections. Three-body continuum discretized coupled-channel calculations were used to determine the effect of the breakup channel on the other reaction mechanisms. The reduced complete and total fusion were found to be hindered above and enhanced below the Coulomb barrier compared with the universal fusion function due to the breakup plus transfer effects.

DOI: 10.1103/PhysRevC.104.024609

I. INTRODUCTION

Over the last three decades, fusion reaction mechanisms involving stable (^{6,7}Li, ^{9}Be) and radioactive (^{6}He, ^{7}Be, ^{8,11}Li, ^{8}B, etc.) weakly bound projectiles have become a subject of great interest in nuclear physics [1,2]. These nuclei, which have special features—cluster structure, "neutron and proton skin" effect and exotic modes of decay [3,4]—are of astrophysical interest because of their role in primordial nucleosynthesis, in chains of capture reactions in massive stars, and in the synthesis of heavy elements [5].

One of the distinctive properties of these nuclei is the high probability of breakup through nuclear (Coulomb) interaction with a light (heavy) target nucleus due to the low binding energy of the last nucleon(s). The influence of this process on other reaction channels like elastic scattering, transfer, or fusion modifies the overall dynamic of the reaction with respect to tightly bound projectiles [6–9]. In addition to the direct complete fusion (CF), there are the incomplete fusion (ICF), when not all breakup fragments are captured by the target, and sequential complete fusion (SCF), when the resulting fragments are separately captured by the target. Another possible outcome is the noncapture breakup (NCBU), in which no fragment is captured. It is important to stress that it is very difficult to experimentally separate ICF from direct transfer reactions and impossible to separate SCF from CF since both processes lead to the same final nucleus. Several experimental and theoretical studies have shown that the influence of the breakup channel manifests in a suppression of fusion for energies above the Coulomb barrier V_C of ≈30% for heavy targets and an enhancement at sub-Coulomb energies [10–25]. It was proved that breakup triggered by transfer has a higher contribution to the total breakup probability than direct breakup at energies below the Coulomb barrier [8,19,23]. Another works claimed that the prompt breakup was responsible for the CF suppression at energies above the barrier [26]. Nevertheless, classical models including lifetimes [8,27] suggest that prompt breakup cannot fully account for all the CF suppression. Moreover, a recent study [27] proposed that the dominant process that leads to CF suppression is direct cluster transfer, a direct consequence of the clustering in weakly bound nuclei. However, a different approach, based on continuum discretized coupled channels calculations, suggests that breakup can explain all the CF suppression [28,29].

Experimentally, exhaustive studies with unstable weakly bound nuclei are complicated to perform due to the low intensities of the radioactive beams. An alternative approach relies on conducting measurements with stable weakly bound nuclei. The most suitable nuclei for this purpose are ^{6,7}Li and ^{9}Be, that have low breakup thresholds between 1.48 and 2.47 MeV. The use of these stable nuclei allows similar studies with higher statistics and precision for several bombardment energies.

In this work we measured $1n$ transfer, CF and ICF for the ^{9}Be + ^{197}Au system for an extended incident energy range, $0.54 \leqslant E_{\rm lab}/V_C \leqslant 1.25$, from offline measurements of β-delayed γ rays. The ^{9}Be structure is represented by a three-body Borromean neutron-halo structure $\alpha + \alpha + n$, similar to ^{6}He and ^{11}Li, with a low energy threshold of $S_n = 1.57$ MeV. Unlike ^{6,7}Li, whose predominant cluster structures are $\alpha + d$ and $\alpha + t$, the case for ^{9}Be is not clear [30–33].

Due to its cluster structure, two reaction mechanisms are possible: (i) breakup of the relatively long-lived ^{8}Be ($\tau = 7 \times 10^{-17}$ s) produced by neutron transfer, and (ii) prompt breakup through $^{9}\text{Be} \rightarrow \alpha + \alpha + n$ or $^{9}\text{Be} \rightarrow ^{5}\text{He} + \alpha$ ($\tau \approx 10^{-21}$ s). The ^{197}Au target was chosen since it presents significant features for fusion and transfer study: (i) half-lives of the evaporation products with timescales of hours, and (ii) a high atomic number ($Z = 79$), which restricts the evaporation channels to the almost exclusive emission of neutrons.

Fusion reactions induced by ^{9}Be projectiles were studied for several target nuclei like ^{12}C [34], ^{19}F [34], ^{27}Al [34], ^{64}Zn [35–37], ^{144}Sm [14,19], ^{168}Er [19], ^{186}W [19], ^{196}Pt [19], ^{202}Pb [12], ^{208}Pb [11,13,38,39], ^{209}Bi [19,20,39,40], and ^{238}U [41].

The fusion of the $^{9}\text{Be} + ^{197}\text{Au}$ system was recently studied by Li *et al.* [42] and Kaushik *et al.* [43] by activation followed by offline measurements of β-delayed γ rays. Li *et al.* obtained CF and ICF cross sections for four energies significantly above the barrier using stacked foil targets. As a main result, they report a CF suppression of about 40% in comparison to couple channel calculations which omit transfer and breakup channels. As the coupling to the breakup channel is responsible for the creation of a repulsive polarization potential in the whole interval around the Coulomb barrier [22], they attribute the observed CF hindrance to this effect. Such a conclusion is further supported through the Universal Fusion Function (UFF) method [44,45], by converting the data to standardized units allowing a comparison with CF measurements of several other systems. In turn, Kaushik *et al.* measured (also via offline counting of β-delayed γ rays) the $^{9}\text{Be} + ^{197}\text{Au}$ CF cross section for energies in the range $E/V_C = 0.82$ to 1.16. Similarly to the previous group, they found a suppression of CF at above-barrier energies of about 39% in comparison to coupled channels calculations. In addition, they also report an enhancement of the CF at below-barriers energies, which they attribute to the deformation of the projectile. This assertion is supported by studying the reduced fusion excitation function and comparing it with the corresponding to other weakly bound projectiles on ^{197}Au targets and with the UFF. According to their results, the ^{9}Be projectile exhibits the largest CF enhancement at subbarrier energies, consistent with the most prominent deformation of this nucleus, in comparison to other weakly bound projectiles for which measurements are available (^{4,6,8}He, ^{6,7}Li, and ^{11}B).

In previous work, we presented experimental data of the elastic and inelastic scattering of ^{9}Be on the ^{197}Au target at several energies around V_C [46]. This data set was described through coupled-channel (CC) calculations, both with Woods-Saxon (W-S) and São Paulo potentials (SPP). Hence, the experimental data presented in this work are part of extensive research aiming to describe the interplay between different reaction channels: elastic and inelastic scattering, direct and compound-nucleus reactions. In particular, we aim to assess the suppression of the CF above and possible enhancement below the barrier in a wider energy range and with a more complete data set than previously measured [42,43]. Therefore, we present an exhaustive study of all reaction channels accessible to the offline detection technique: neutron-stripping, neutron-pickup, and complete and incomplete fusion. These channels were described over the whole measured energy range within a consistent CC formalism.

The present work is organized as follows: in Sec. II the experimental setup is described in full detail and CF, ICF and transfer cross sections are presented. In Sec. III coupled channel, coupled reaction channel, and continuum discretized coupled-channel results for the elastic and inelastic, $1n$ transfer, and elastic breakup, respectively, are compared with the experimental data. The effect of the breakup plus transfer channels on CF and ICF is also studied. The summary and conclusions are given in Sec. IV.

II. EXPERIMENTAL SETUP

Cross section for the CF, ICF and one-neutron transfer channels were measured for the $^{9}\text{Be} + ^{197}\text{Au}$ system at 33 bombarding energies between 22 and 50.5 MeV at the TANDAR Laboratory in Buenos Aires, Argentina. The nominal value of the Coulomb barrier was estimated to be $V_C^{\text{lab}} = 40.5$ MeV ($V_C^{\text{c.m.}} = 38.7$ MeV) based on empirical models [47]. ^{9}Be beams obtained from the 20 UD tandem accelerator impinged on ^{197}Au target foils placed at the center of a 70-cm diameter scattering chamber. The targets were around 200 (300) μg/cm^2 for lower (higher) bombarding energies. These values were selected as a compromise between a high reaction rate and a low spread in the reaction energy. The target angle was set at 0° relative to the beam direction. Two silicon monitor detectors, placed at $+16°$ and $-16°$ where scattering is pure Rutherford, where used for normalization purposes. The beam was defined by a set of two rectangular collimators (7 mm × 9 mm) located 51 and 156 cm upstream the scattering chamber and a third circular collimator with a diameter of 7.6 mm placed at the entrance of the scattering chamber, as set up previously in Ref. [46].

An aluminum catcher of about 200 μg/cm^2 was placed behind the target, at an approximate distance of 1 mm in the same target holder. This material was chosen because the γ rays emitted by the main fusion-evaporation products of $^{9}\text{Be} + ^{27}\text{Al}$ are short lived in comparison with the products of interest. Therefore, they do not produce interference in the offline measured spectra. The catcher thickness was selected, based on SRIM simulations [48], to stop possible fusion residues and transfer recoils from the $^{9}\text{Be} + ^{197}\text{Au}$ system, while it still lets the elastic scattered beam particles pass through. The catcher is also thin enough to avoid the residues from the $^{9}\text{Be} + ^{27}\text{Al}$ reaction to be retained within it.

A new set of target and catcher foils were used for each bombarding energy. This method was previously used by our group to measure the fusion and transfer cross sections of the $^{10}\text{B} + ^{197}\text{Au}$ system [49]. A Faraday cup at the end of the beam line, 6 m away from the scattering chamber, is used to obtain the beam profile. The integrated charge collected in time intervals of 1 s, as well as the number of events in the monitors are digitally recorded. Typical irradiation time was between 2 to 10 h, according to the beam intensity and the half-lives of the products of interest.

Upon completion of irradiation, the target and catcher were removed from the scattering chamber by the use of a target extraction device. This allowed the safe extraction of targets

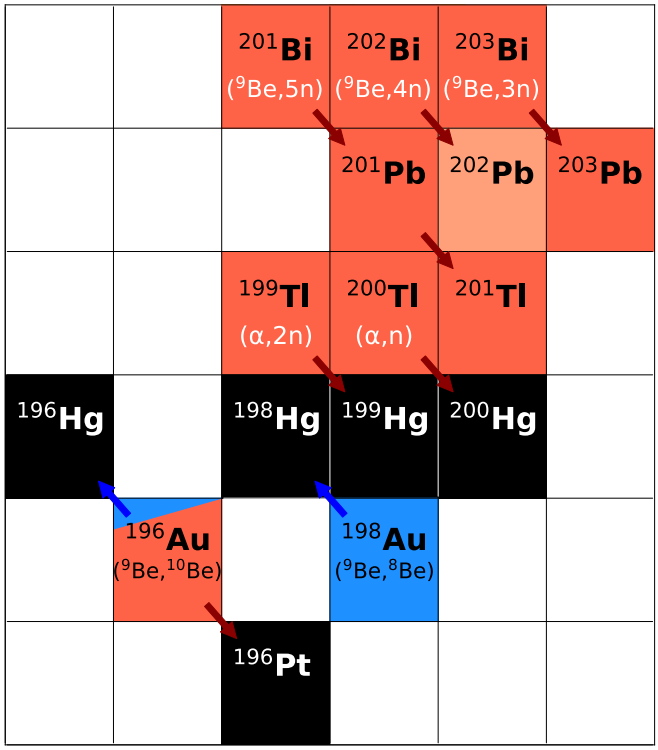

FIG. 1. Decay scheme of the CF and ICF compound nuclei and transfer products identified in the γ spectrum. Stable nuclides are depicted in black. Red colored nuclides decay via β^+ and/or electron capture, whereas the blue colored nuclei decay via β^-. ^{202}Pb, with a half-life too long to be detected (53 ky), is depicted in light red. (α, x) stands for the ICF following the ^{9}Be prompt breakup.

to the atmosphere within a few minutes without loosing the vacuum condition in the scattering chamber. The time consumed in this process was on the order of 10 min, measured to the precision of a hundredth of a second and was taken into account for the calculation of the cross sections. Both target and catcher were then placed at a fixed distance in front of a 40%-efficiency, high-purity germanium detector with 2.1 keV energy resolution at 1332.5 keV. The efficiency was determined by the γ radioactive sources ^{133}Ba (0.056 μCi), ^{152}Eu (0.020 μCi) and ^{60}Co (0.070 μCi). The detector was shielded by a lead castle with an outer cover of cadmium and paraffin. The activity measurements spanned from 2 to 10 h, depending on the expected channel cross sections following irradiation at each bombarding energy.

The neutron transfer can produce either the ^{198}Au (neutron stripping) or ^{196}Au (neutron pickup). ^{198}Au go through β^- to produce ^{198}Hg. On the other hand, ^{196}Au decays mainly through ϵ to ^{196}Hg or, on a minority basis, via β^- to produce ^{196}Pt (see Fig. 1). It must be noted, that ^{9}Be breakup followed by neutron capture by the target can also contribute to the formation of ^{198}Au.

Predictions of the main fusion-evaporation channels and relative yields were obtained by the PACE2 [50] statistical code for each incident energy. The level-density parameter was $a = A/K$ where A stands for the mass number and K was varied between 7 and 10. The angular momentum (l) distribution was obtained from CC calculations performed on the elastic and inelastic angular distributions from Ref. [46] (see Sec. III). The results are presented in Fig. 4 (full table with experimental data is available in the Supplemental Material [61]). Best agreement with the experimental data was found for the value of $K = 9$, in concordance with Kaushik [43].

Results for the CF of the ^{9}Be + ^{197}Au system show that the compound proton-rich ^{206}Bi nucleus decays mainly through neutron evaporation (xn). Within the energy range of 35 and 50 MeV (0.88V_C and 1.25V_C), the $3n$(^{203}Bi) and $4n$(^{202}Bi) channels are the dominant processes; while the $5n$(^{201}Bi), more energetic, becomes significant for energies greater than 45 MeV. In contrast, the $2n$(^{204}Bi) channel is a minor one and is only present in a limited range of energies close to V_C. Experimentally, this channel could not be detected. PACE2 also predicts the contribution from neutron-proton evaporation channels pxn ($n = 2, 3$) to produce ^{202,203}Pb. However, the impact on the σ_{CF} is <1% virtually in all incident energies. Furthermore, ^{202}Pb, which has the highest yield of both, decays by ϵ with a half-life of $T_{1/2} = 52.5 \times 10^3$ y and renders it impossible to detect.

The calculation of evaporation channels following ICF with PACE2 were carried out considering the approximate energy of the α particles as $E_\alpha = (4/9)E_{\rm lab}(^9\text{Be}) - S_n$ [14], where S_n is the neutron separation energy of the ^{9}Be.

Absorption of an α particle produces ^{201}Tl, that may undergo evaporation of one or two neutrons to render the ^{199,200}Tl isotopes. ^{201}Tl can also decay by ϵ to ^{201}Hg with $T_{1/2} = 3.0421$ d, although this was not detected in the γ-ray spectra. Fusion following prompt breakup can also produce the ^{202}Tl isotope which subsequently evaporates two or three neutrons leading to the same thallium isotopes. Both Bi and Tl isotopes from CF and ICF decay through electron capture $p + e \rightarrow n + \bar{\nu}_e$ to produce ^{202,203,204}Pb and ^{199,200}Hg and their corresponding γ rays are measured offline. In turn, lead isotopes, except the very long half-life ^{202}Pb, decay through electron capture to ^{201,203}Tl. In Fig. 1 a section of the table of isotopes is displayed, corresponding to the evaporation residues and decays of the involved channels.

As a summary, in Table I the intensity of the principal γ rays and half-lives of each measured channel is presented. Only the main decay channel for the ^{196}Au is presented.

An example of a γ-ray spectrum of the target and catcher is presented in Fig. 2 for an incident energy of 48 MeV. As can be seen, at this incident energy, all the evaporation channels are active. Each peak is identified by its energy and their decay level scheme. Other peaks identified were those corresponding to the ^{24}Na decay, produced by reactions in the catcher foils [59], ^{40}K [60] and the 511 keV from electron-positron annihilation. A complementary identification was performed through half-life determination. Time bins between 8 and 32 min were used, depending on selected half-life nucleus. An energy gate was set around the peak. In cases where there are more than one peak, we use the branching ratio as an extra measure for confirmation. In Fig. 3, the number of γ events per unit time is displayed for a peak belonging to each channel considered. The half-lives calculated are in agreement with the tabulated values referenced in Table I, except for the peak of 355.7 keV that could not be calculated, since its half-life

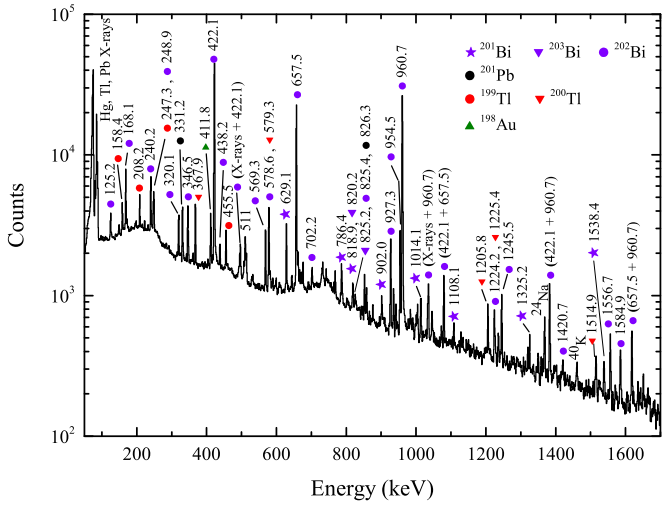

FIG. 2. Offline γ-ray spectrum measured from an activated set of target plus catcher at an incident energy of 48 MeV.

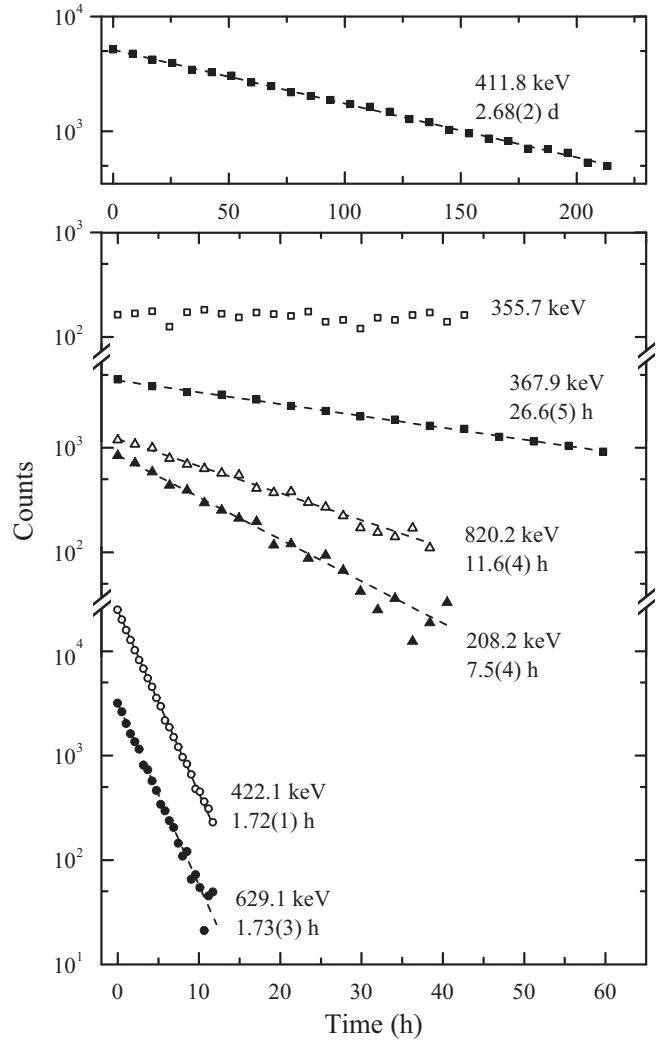

FIG. 3. Activity of the main produced nuclei as a function of time. An exponential decay fit was performed to extract half-life values for each reaction channel. All resulting values are in agreement with those in Table I.

TABLE I. Main channels from the n transfer, CF, and ICF for the ^{9}Be + ^{197}Au system including reaction Q values and decay features. The half-lives ($T_{1/2}$), principal γ rays, and intensity of the decay processes were obtained from Refs. [51–58].

Channel	Q (MeV)	Decay	$T_{1/2}$	E_γ (keV)	I_γ (%)
		n transfer			
(^{9}Be, ^{8}Be)	4.8	^{198}Au → ^{198}Hg	2.69 d	411.8	95.6
(^{9}Be, ^{10}Be)	−1.3	^{196}Au → ^{196}Pt	6.17 d	355.7	87.0
		Complete fusion			
(^{9}Be, 3n)	−22.5	^{203}Bi → ^{203}Pb	11.76 h	820.2	30.0
				825.2	14.8
(^{9}Be, 4n)	−31.3	^{202}Bi → ^{202}Pb	1.71 h	422.1	83.7
				657.5	60.6
				960.7	99.3
(^{9}Be, 5n)	−38.7	^{201}Bi → ^{201}Pb	103 min	629.1	26.0
		Incomplete fusion			
(α, n)	−9.7	^{200}Tl → ^{200}Hg	26.1 h	367.9	87.0
				1205.8	29.9
(α, 2n)	−16.8	^{199}Tl → ^{199}Hg	7.42 h	208.2	12.3
				455.5	12.4

is too long in comparison with the measuring time intervals adopted.

The expression for the total cross section is

$$\sigma = \frac{N_D}{I\varepsilon_f(\epsilon)} \frac{\sigma_{\text{Ruth}}}{(e^{-\lambda t_i} - e^{-\lambda t_f})} \frac{1}{\int_0^{t_{irr}} e^{\lambda t'} N_{\text{M}}(t')dt'}, \quad (1)$$

where σ_{Ruth} groups the Rutherford differential cross section at the monitor angle, its solid angle and the Jacobian factor for the laboratory to center-of-mass transformation:

$$\sigma_{\text{Ruth}} = \frac{d\sigma_{\text{Ruth}}}{d\Omega}(\theta_M)\frac{\Omega_{\text{M}}}{J(\theta_M)}. \quad (2)$$

The solid angle values of the two monitors were extracted from Ref. [46]. The remaining parameters in Eq. (1) are the decay constant $\lambda = \ln(2)/T_{1/2}$, the number of γ events in the peak N_D, the number of elastic scattered ^{9}Be particles per time unit $N_{\text{M}}(t')$, the γ relative intensity I, the efficiency $\varepsilon_f(\epsilon)$ of the HPGe detector at a given γ-ray energy, the irradiation time t_{irr} and, finally, the initial and final times of measurement t_i and t_f.

The number of γ events in each peak was obtained by fitting a Gaussian distribution. The cross sections calculated by using each of the two monitors were averaged and this value was subsequently weighted-averaged with the other cross-section values corresponding to the other γ rays, corresponding to the same channel of Table I, to obtain the final σ value for that channel. Uncertainties were calculated taking into account N_D, $N_{\text{M}}(t')$, $\varepsilon_f(\epsilon)$ and monitor solid angle contributions, ranging between 3% and 20%. The current per-unit-time $i(t)$ collected by the Faraday cup was discretized by a counter and used as an independent method to corroborate the normalization. The summary of the experimental excitation functions for n-transfer channels (pickup and stripping),

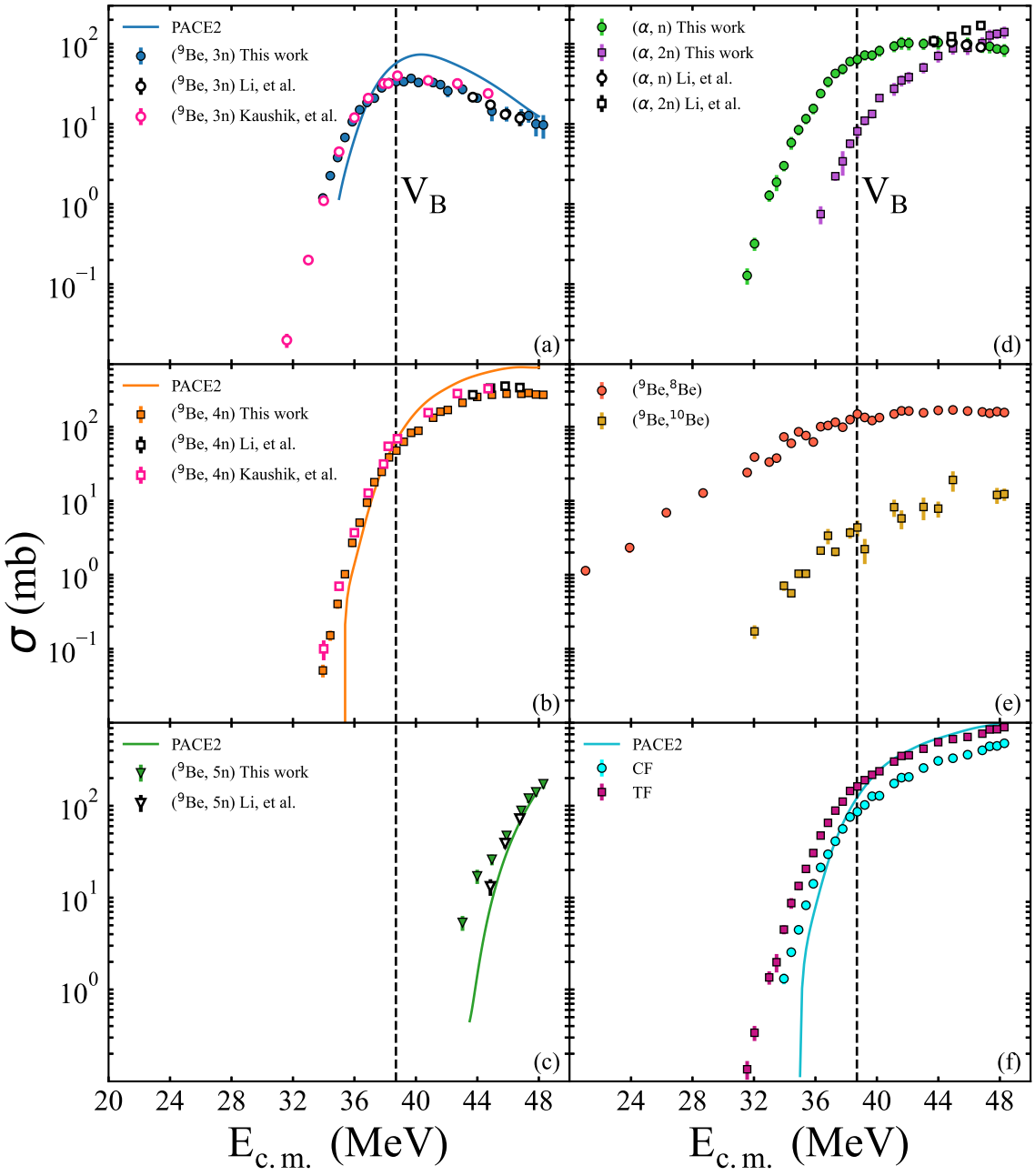

FIG. 4. Experimental cross sections (full symbols) for the CF, ICF, and n-transfer channels measured for the ^{9}Be + ^{197}Au system. In solid lines, PACE2 calculations are included for the CF neutron evaporation channels. Cross sections obtained by Li *et al.* [42] and Kaushik *et al.* [43] are also included (open symbols). Finally, in bottom right panel, CF and TF (CF + ICF) cross section are presented. σ_{CF} were corrected based on PACE2 calculations of the ratio $\sigma_{3n+4n+5n}/\sigma_{\rm fus}$.

CF and ICF for the ^{9}Be + ^{197}Au system are displayed in Fig. 4 (The full table with the experimental data is available in the Supplemental Material [61].). The results obtained by Li [42] and Kaushik [43] for CF and ICF are also shown for comparison. It is important to point out the relatively high cross-section values of the ^{198}Au production for higher energies and its slow decrease as the energy diminishes, even at energies down to about half the Coulomb barrier. ^{9}Be breakup followed by neutron capture may significantly contribute to the formation of ^{198}Au at these low energies.

Comparing the results for the xn channels presented in this work with those obtained by Refs. [42] and [43], we found an excellent agreement for the 3n evaporation channel in all the energy range [Fig. 4(a)]. On the other hand, for

the $4n$ [Fig. 4(b)], our results at the highest incident energies were ≈20% lower than in Refs. [42] and [43], while for the more energetic $5n$ [Fig. 4(c)], they were ≈18% higher than in Ref. [42]. Concerning the ICF channels displayed in Fig. 4(d), the αn cross sections measured are compatible with the data of Ref. [42], but the $\alpha 2n$ ranged between 19% and 60% lower. Due to the reduced energy range studied by Ref. [42] (as in channel $4n$), it was unclear whether these differences are energy dependant or systematic.

Finally, CF and TF (CF + ICF) are displayed in Fig. 4(f). The results from PACE2 indicated than neutron evaporation channels account approximately for 99% of the CF cross section (considering also fission) within the incident energy interval of the experiment. To take into account the contribution of the nonmeasured channels, the CF cross sections were corrected by the ratio of the sum of the xn ($x = 3, 4, 5$) channels and the total cross section obtained by PACE2: $R = \sum_{x=3}^{5}(\sigma_{xn}^{\text{pace}})/\sigma_{\text{fus}}^{\text{pace}}$. Hence, the corrected CF cross sections are $\sigma^{\text{corr}} = \sigma^{\text{expt}}/R$. The R factor was calculated for all incident energies, the results ranged between 94% and 98%. For the ICF cross-sections, no corrections were needed since neutron evaporation (^{9}Be, $\alpha 2n$) and (^{9}Be, $\alpha 3n$) contributions are significantly less than 1% for all energies considered.

III. THEORETICAL ANALYSIS

In the previous work [46], a CC analysis has been presented to describe the elastic and inelastic differential cross sections. A good agreement of the data was achieved. However, coupled-channel calculations using Woods-Saxon (W-S) potentials have many free parameters that need to be adjusted to describe the studied cross sections. In the present work, the São Paulo Potential (SPP) systematics [62] was used to describe the elastic and inelastic differential cross sections, and then it was used to analyze the one-neutron transfer cross sections.

The theoretical cross sections were obtained by performing CC calculations, considering the ground state (g.s.) of ^{9}Be and the first six states of the ^{197}Au. The double folding SPP [63] was used in both real and imaginary parts of the optical potential [$U = (1.0 + iN_i)V_{SP}$]. N_i is a strength coefficient of the imaginary part. The value $N_i = 0.60$ was used to account for the loss of flux to the absorptive channels, as couplings to continuum channels are not explicitly considered in the coupling scheme. To account for the target's collective states, the transition probabilities of Ref. [64] have been used. All the calculations were performed using the FRESCO code [65].

As can be seen from Fig. 5, the elastic differential cross sections calculated with the SPP systematics agree pretty well with the experimental data, as reported in the previous work [46]. On the other hand, the experimental data corresponding to the 279.0 keV ($5/2^+$) state was underestimated by the previous work [46]. In the same work, it has been stated that the 279.0 keV ($5/2^+$) and 270.0 keV ($3/2^+$) states cannot be experimentally resolved. Thus, summing the differential cross sections of these two states, a better agreement with the experimental data with the theoretical results is achieved, as shown in Fig. 6. This leads us to conclude that the results for the differential cross sections using the SPP have a better

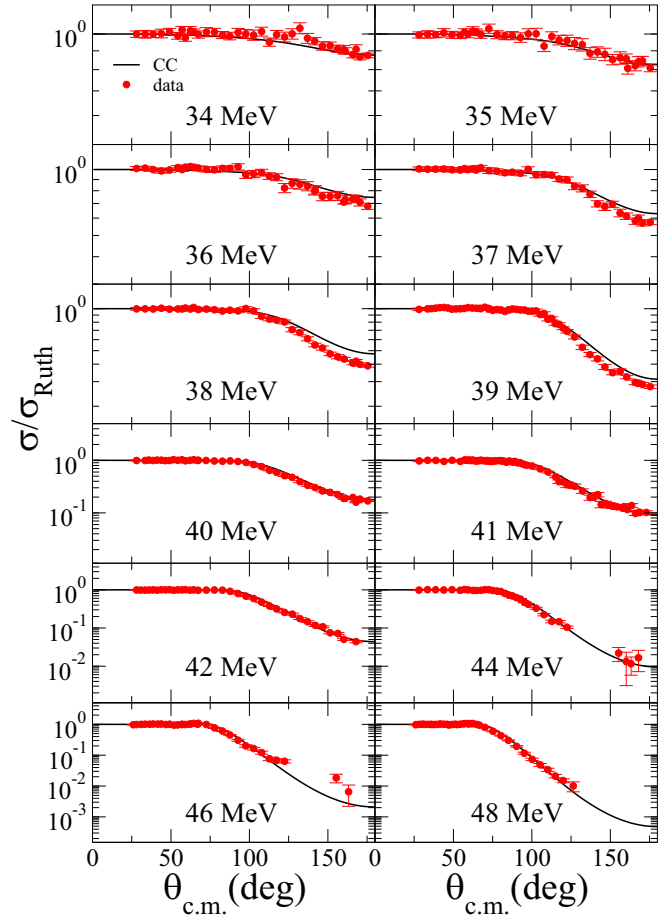

FIG. 5. Comparison between the experimental data and the theoretical CC calculations for the elastic scattering.

agreement with the reported data. Making a step forward in the theoretical analyses, the one-neutron transfer (pickup and stripping) and breakup reactions will be described in the following subsections.

A. One-neutron stripping reaction

To study the ^{197}Au(^{9}Be, ^{8}Be)^{198}Au stripping transfer reaction, we used the coupled reaction channel (CRC) method. The entrance partition uses as a base the CC calculations. However, in the outgoing partition, as we do not explicitly consider the couplings between final partition states, the N_i strength coefficient was set equal to 0.78. This coefficient was proved to be appropriate for describing the elastic-scattering cross section for many systems in a wide range of masses and energies [66]. The transition probabilities of collective states of the target are the same as used in the CC calculations.

W-S form factors were used to generate single-particle wave functions. The depth of these potentials was adjusted to fit the experimental one-neutron separation energies. The reduced radii and diffuseness were set equal to standard values as 1.25 and 0.65 fm, respectively, for binding the neutron to the ^{8}Be and ^{197}Au cores. The nonorthogonality corrections, prior representation, and full complex remnant approximations were adopted in CRC calculations. The CRC

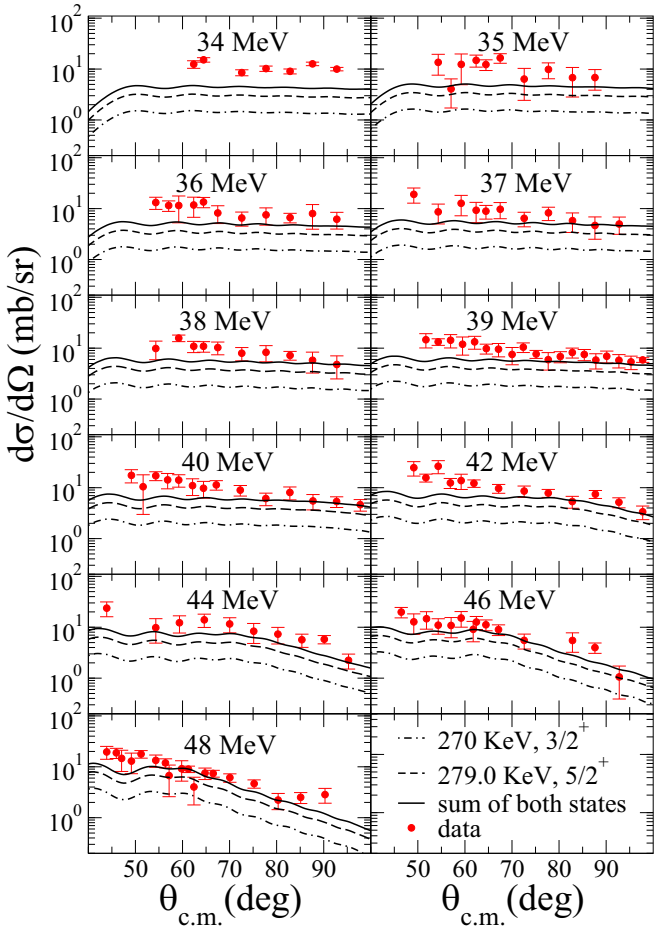

FIG. 6. Comparison between the experimental data with the theoretical inelastic calculations. The dashed lines represent the cross section of 279.0 keV ($5/2^+$) and the dash-dotted line represents the 270.0 kev ($3/2^+$) states of ^{197}Au.

calculations adopted here were performed for several systems [67–80], reproducing the experimental cross sections for the one- and two-neutron transfer reactions with great success.

The spectroscopic amplitudes for the $\langle^9\text{Be}|^8\text{Be}\rangle$ projectile overlaps were taken from Ref. [77]. Due to computational limits, we were not able to calculate the spectroscopic amplitudes for the $\langle^{197}\text{Au}|^{198}\text{Au}\rangle$ target overlaps. For this reason, they were set equal to 1.0. The coupling schemes for the projectile and target overlap corresponding to the one-neutron stripping transfer reactions are sketched in Fig. 7. All the states up to 703 keV for the target overlaps are represented in this coupling scheme. The block of states in the rightmost is separated only for clarity. They represent a continuation of ^{198}Au excited states, and every single arrow represents the overlaps to all of these states.

The CRC results for the one-neutron stripping excitation function are compared in Fig. 8 with the experimental data measured in the present work. The results coupling states up to 703 keV of the ^{198}Au in the one-neutron stripping reaction channel are represented by the solid red curve [CRC up to 703 keV (^{198}Au)]. The main contribution to the transfer cross sections came from the coupling to the first resonant state (2^+3.03 MeV) of the ^{8}Be with some states (g.s., 236, 328, 381, 450, 482, 511, 529, 548, 625, 637, and 702 keV) of the residual nucleus ^{198}Au. The inclusion of this resonance state has shown not to be important in the case of the two-neutron transfer reaction ^{9}Be(^{7}Be, ^{9}Be) ^{7}Be [77], but it is very important for the reaction studied in this work. The contribution of these more relevant states is represented by the dashed green curve [CRC more imp. states (^{198}Au)] in Fig. 8. They are responsible for about half of the total transfer cross section. The cross section was always greater when the ejectile was in its 2^+ resonant state than when it was in its g.s., for all the states of the residual nucleus. For the two lower energies studied in the present work (22 and 23 MeV, which are nearly half of the Coulomb barrier), the contribution to the cross section came about the same from all states considered in the coupling scheme. The more states were included in the coupling scheme, the better is the description of the experimental data. Due to computational limitations, it was not possible to add more states above 0.703 keV.

To consider the effect of the breakup channel in the transfer calculations, we performed a continuum discretized coupled-channel (CDCC) calculation. The objective was to derive a polarization potential ($U_{\text{pol}} = V_{\text{pol}} + W_{\text{pol}}$) that could trace back the breakup effect on the elastic and indirectly on the transfer cross section. In this calculation, a neutron in the $1p_{3/2}$ shell is coupled to a ^{8}Be core with a breakup threshold of $S_n = 1.6$ MeV. This is the most probable breakup channel for the ^{9}Be projectile, although it may also break into $\alpha + {}^5$He with $S_\alpha = 2.31$ MeV. The SPP with $(1 + iN_i)$ strength coefficients was used to describe the core-target interaction ($^8\text{Be} + {}^{197}\text{Au}$). For the $n + {}^{197}$Au interaction, the potential was taken from Ref. [81], which has proved to be very suitable to describe this interaction for a stable nucleus.

The binning method was used to describe the continuum. Bins considering s, p, and d n-core relative angular momentum with maximum bins energy of 8 MeV with a step of 0.5 MeV from 0 to 2.0 MeV and step of 2.0 MeV from 2.0 to 8.0 MeV were used. For the f waves, we considered the step of 2.0 MeV from 0.0 up to 8.0 MeV. The interaction potential was expanded in multipoles considering up to the octupole term. The interaction form factors were derived by integrating by the projectile internal distances up to 250 fm. This value also guaranteed the orthogonality among bin states. The bins were generated by using potential parameters taken from Ref. [82]. The coupled equation was integrated numerically up to 1000 fm and the maximum projectile-target angular momentum considered was $500\hbar$.

In Fig. 9, we show, as an example of the convergence obtained, the cross section for each angular momentum considered up to the f wave. One observes that the f wave ($5/2^-$ and $7/2^-$) has the lower contribution while the s, p, and d waves ($1/2^+$, $1/2^-$, $3/2^-$, $3/2^+$, $5/2^+$) have the main contribution to the cross section. In the inset to Fig. 9, the real and the imaginary parts of the polarization potential around the Coulomb barrier (about 11 fm) are shown. As expected [1], its real part is repulsive while the imaginary part is absorptive. The results shown in Fig. 9 correspond to an incident energy of 40 MeV. However, they remain valid for the entire energy range studied in this work.

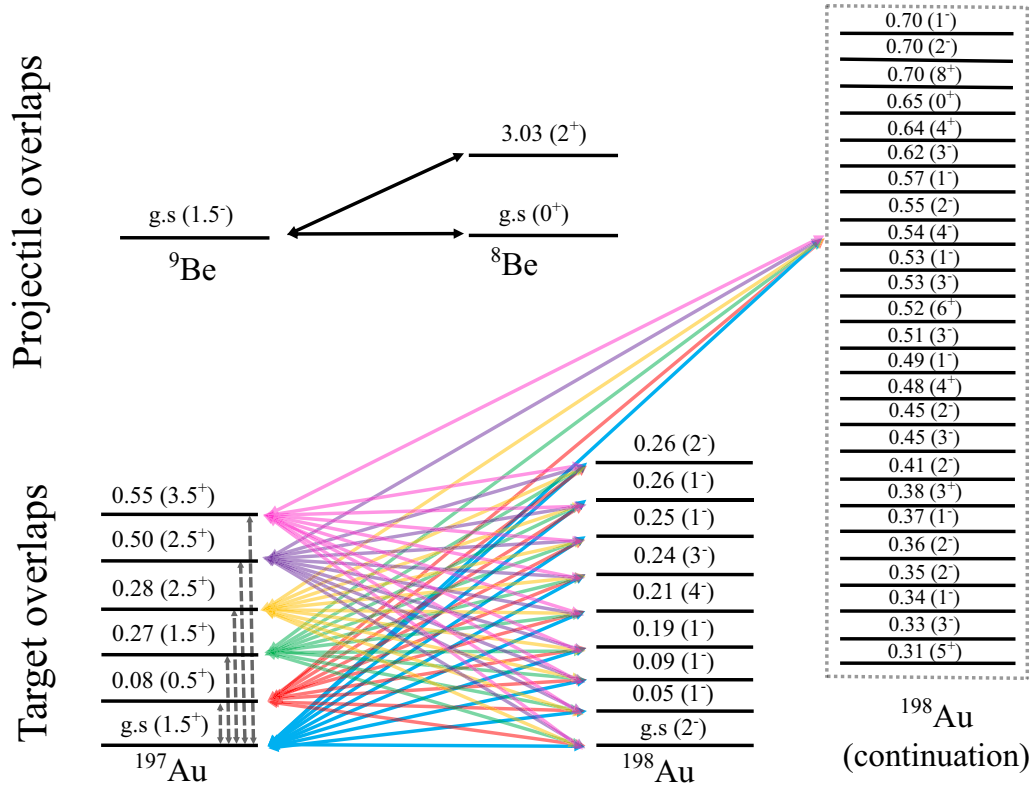

FIG. 7. Coupling scheme of the projectile and target overlaps used in the one-neutron stripping transfer reaction calculations.

Thereby, the polarization potential was added to the CRC calculations, which included the main states. The results for the one-neutron stripping reaction are shown by the black dashed-dotted curve in Fig. 8. When this polarization potential is added, one needs to substitute the $i0.6V_{SP}$ we had in the entrance partition with an internal imaginary potential to absorb the flux inside the Coulomb barrier (corresponding exclusively to fusion). Otherwise, we would have double counting of the effect of the breakup channel on the elastic. This internal W-S potential usually has the parameters: $V = 50$ MeV, $r = 1.06$ fm, and $a = 0.2$ fm for the depth, reduced radius, and diffuseness, respectively (although the fusion cross section is almost independent of the choice of these parameters [83]). Due to the small value of the polarization potential close to the barrier radius, of the order of 0.1 MeV for higher energies, the breakup channel does influence the transfer cross section. The comparison between the CRC calculations including the breakup dynamic polarization potential, which needs to include an internal potential, and the CRC calculations only with the internal potential shows that the increment of the cross sections for energies above 35 MeV (when compared with the green dashed curve) is due to the internal imaginary potential and not due to the polarization potential.

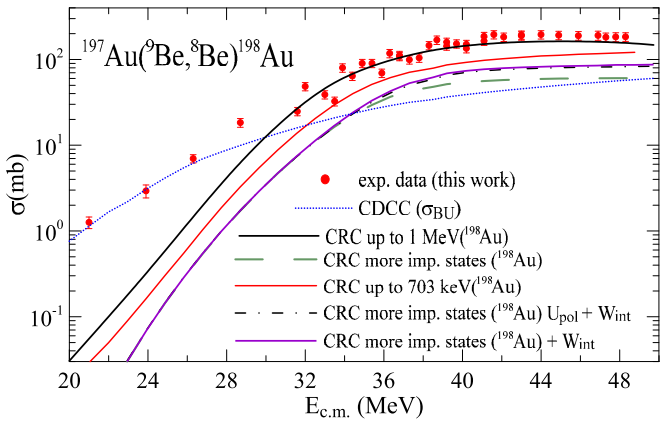

FIG. 8. Comparison between the experimental data with the theoretical one-neutron transfer and elastic breakup cross section.

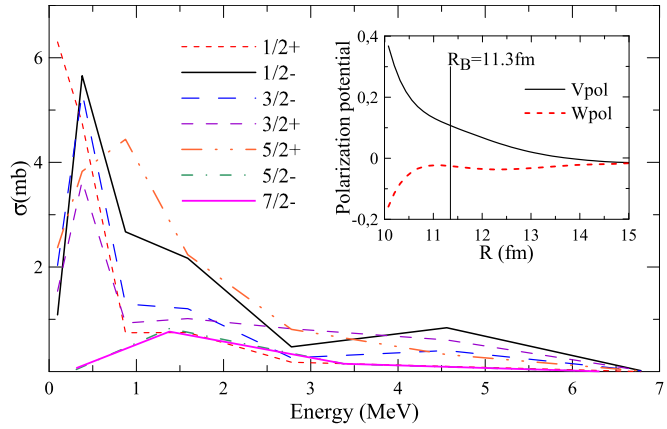

FIG. 9. Comparison between all the waves considered in the CDCC calculations. The inset shows the polarization potential close to the barrier radius, both for 40 MeV.

TABLE II. Spectroscopic amplitudes used in the CRC calculations for one-neutron pickup reaction.

Initial state	j	Final state	Spect. amp.
$^{9}\mathrm{Be}_{\mathrm{g.s}}(3/2^{-})$	$(1p_{1/2})$	$^{10}\mathrm{Be}_{\mathrm{g.s}}(0^{+})$	−1.582
$^{9}\mathrm{Be}_{\mathrm{g.s}}(3/2^{-})$	$(1p_{1/2})$	$^{10}\mathrm{Be}_{3.368}(2^{+})$	−0.159

From Fig. 8, it is observed that the theoretical curve does not follow the shape of the experimental values for the lower energies (below 32 MeV). In our experimental setup, is not possible to determine if the neutron is absorbed by the target after ^{9}Be breaks. Figure 8 seems to indicate that this is the situation for incident energies much lower than the Coulomb barrier. The blue dotted curve represents the elastic breakup cross section derived from our CDCC calculations that, perhaps by chance, coincides with what we call a one-neutron transfer cross section. It is observed that the breakup probability without the absorption of any of the fragments is very high and dominant at this energy regime. This guides us to infer that the neutron produced by the breakup might also be absorbed with high probability and produce this high cross section for the $^{8}\mathrm{Be} + {}^{198}\mathrm{Au}$ partition at this energy regime. This assumption needs to be supported by additional theoretical calculations out of the scope of the present work. The measurement of angular distributions might also elucidate this situation because both reaction mechanisms would produce different angular distributions.

We also studied the effect of the inclusion of the one-neutron pickup channel on the one-neutron stripping cross section. The effect was minimal, and for this reason, we did not include it in Fig. 8.

B. One-neutron pickup reaction

The CRC method was also used to study the ^{197}Au (^{9}Be, ^{10}Be) ^{196}Au pickup transfer reaction. Like the stripping process, the calculations used as a base the CC calculations, and the strength factors for the real and imaginary parts of the optical potential remained the same. The W-S form factors adopted here are also the same as those used in the stripping case. As we cannot calculate, due to computational limits, we assumed that the spectroscopic amplitudes for the $\langle {}^{197}\mathrm{Au}|{}^{196}\mathrm{Au}\rangle$ overlaps are 1.0 for all configurations.

The spectroscopic amplitudes for the $\langle {}^{9}\mathrm{Be}|{}^{10}\mathrm{Be}\rangle$ overlaps were derived by performing shell-model calculations with the NuShellX code [84]. To obtain the projectile overlaps the *ps-dpn* model space and effective interaction *psdmod* were used. This interaction was generated from a modification of the psdwbt interaction [85]. The Hamiltonian is similar to the one used by Warburton, Brown, and Millener (WBM) to describe the excited states of ^{16}O [86]), where they used a two-body Hamiltonian that gives a global fit to *p-sd*-shell nuclei. The ^{4}He is considered as a closed core and the $1p_{1/2}$, $1p_{3/2}$, $1d_{3/2}$, $1d_{5/2}$, $2s_{1/2}$ orbitals are taken as the valence space for protons and neutrons. The spectroscopic amplitudes obtained in this calculations are shown in Table II, and the coupling scheme for the overlaps is sketched in Fig. 10.

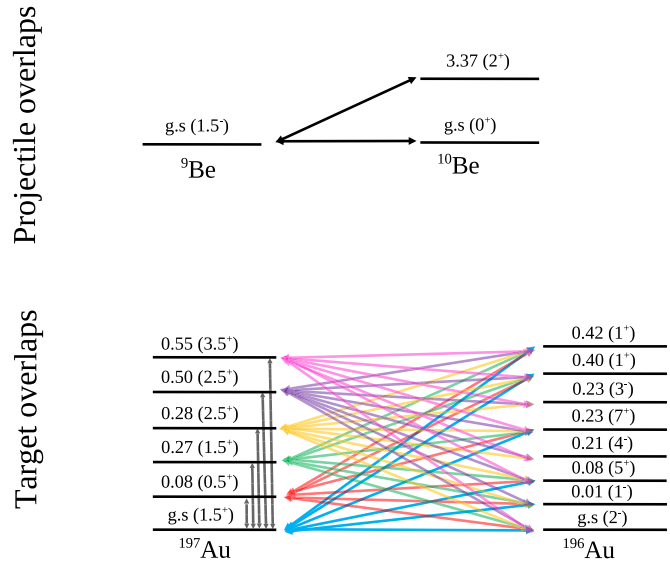

FIG. 10. Coupling scheme of the projectile and target overlaps used in the one-neutron pickup reaction calculations.

The theoretical cross sections for the one-neutron pickup have quite a good agreement with the experimental data, as shown in Fig. 11. The contribution of each state to the cross section varies with the bombarding energy. In this reaction, the g.s. and the 0.01 MeV (1^{-}) state of residual ^{196}Au are the states that have more contribution at energies below the Coulomb barrier. Above the Coulomb barrier, the 0.08 MeV (5^{+}) state becomes very relevant. Unlike the stripping process, the first-excited state of the ^{10}Be ejectile does not contribute to the one-neutron pickup cross section. The cross section for the states of the system leading the ejectile in this excited state is about three orders of magnitude smaller than when the ejectile remained in the g.s. However, the small overestimation of the experimental one-neutron pickup cross section might be originated by the values of the spectroscopic amplitudes adopted for the target overlaps, which were not calculated

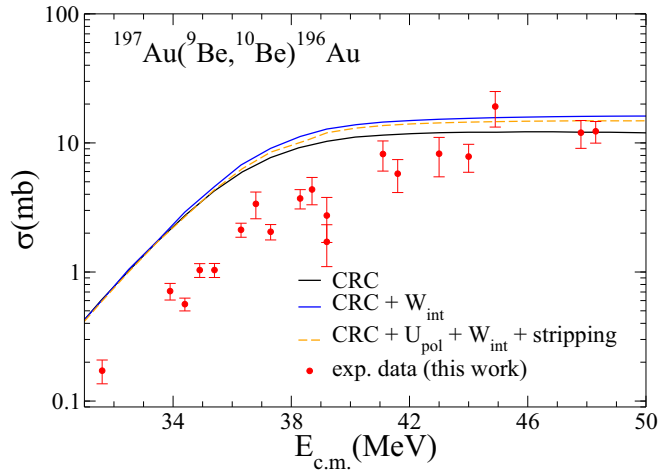

FIG. 11. Comparison between the experimental data with the theoretical one-neutron pickup calculations.

microscopically due to computational limits. The couplings with the stripping process and the inclusion of the breakup dynamic polarization potential do not significantly affect the pickup cross section, as one can see from Fig. 11. The difference between the curves arises from the use of internal potential in the imaginary part of the optical potential when the dynamic polarization potential was included (a detailed discussion is given in the previous subsection).

C. Fusion

The fusion process can be strongly affected by the breakup channel. One way to estimate its effect is to compare the experimental fusion data with the CC calculations that include the most important channels, except for the breakup channels. The CC calculations represented here are very similar to those used at the beginning of this section. The only difference lies in the imaginary part of the optical potential. There, the imaginary part of the optical potential consisted of $i0.6V_{SP}$. When one is interested in deriving the fusion cross section, an imaginary W-S potential internal to the barrier has to be used instead. Again, the depth, reduced radius, and diffuseness adopted were $W = -50$ MeV, $r_w = 1.06$ fm, and $a_w = 0.2$ fm, respectively.

Another way to study the effect of the breakup channels on fusion cross sections is by comparing experimental data for tightly bound and weakly bound systems. For this purpose, the experimental data have to be reduced, and a benchmark function is highly desired. The universal fusion function (UFF) method [44,45] fulfills all these requirements. This method consists in reducing the data by using the following procedure:

$$E_{\text{c.m.}} \to x = \frac{E_{\text{c.m.}} - V_B}{\hbar\omega}, \quad \sigma_F \to F(x) = \frac{2E_{\text{c.m.}}}{\hbar\omega R_B^2}\sigma_F, \quad (3)$$

where the $E_{\text{c.m.}}$ is the energy in the center-of-mass frame, V_B is the Coulomb barrier, σ_f is the fusion cross section, R_B and $\hbar\omega$ are the radius and curvature of the Coulomb barrier, respectively. One can apply this reduction method to Wong's formula [87], giving the UFF:

$$F(x) = \ln[1 + \exp(2\pi x)]. \quad (4)$$

The UFF is system-independent. However, this formula has some shortcomings. To overcome these problems, Canto *et al.* [44,45] use the renormalized fusion function

$$\bar{F}_{\text{expt}} = F_{\text{expt}}\frac{\sigma_F^W}{\sigma_F^{CC}}, \quad (5)$$

where σ_F^W, and σ_F^{CC} are the fusion cross sections calculated by Wong's formula and CC calculations, respectively. With this modification, it is expected that the renormalized experimental data deviations from the UFF are caused by the channels not included in CC calculations (usually the breakup + transfer channels). It is important to choose a reliable potential (like a double-folding potential) to derive the barrier parameters. Of course, the results will depend on these parameters.

In Figs. 12 and 13, the reduced CF and TF cross sections for some heavy systems having ^{9}Be as a projectile are compared with the UFF. The linear scale is used to study the effect of the nonincluded channels at energies above the Coulomb barrier. Contrarily, the logarithmic scale is used to study those effects below the Coulomb barrier.

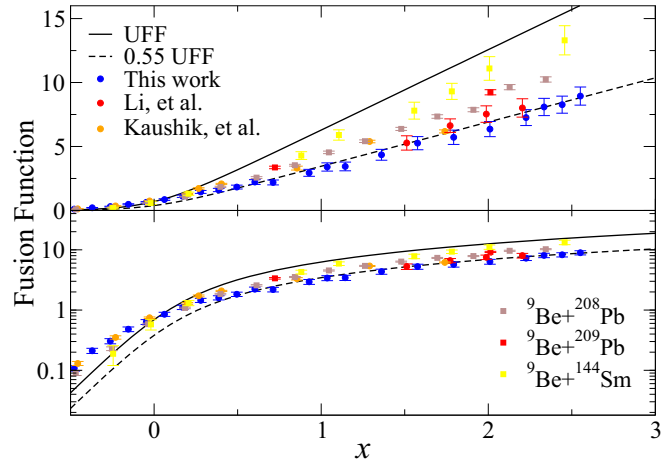

FIG. 12. Comparison between the UFF and renormalized fusion function for total fusion (CF). The systems are composed by the ^{9}Be projectile on different targets: ^{186}W [88], ^{144}Sm [89], ^{208}Pb [13], ^{197}Au from Refs. [42,43] and this work.

From Fig. 12, one can see the enhancement of the CF experimental data at subbarrier energies and the hindrance for energies above the Coulomb barrier (represented by $x = 0$). These results are in agreement with the systematic for the reduction function method for heavy systems, as discussed in Ref. [44], where it is expected a suppression in a range of 30%–35%. However, the hindrance for the system studied in the present work is slightly greater, about 45%, compared with the UFF. The ^{9}Be + ^{208}Pb [13],^{144}Sm [89] systems show the suppression in the expected range, but the ^{9}Be + ^{186}W [88] shows the same hindrance as the present experimental data. The reduced CF for the ^{9}Be + ^{197}Au from Li [42] and Kaushik [43] present a hindrance of the same magnitude as our data.

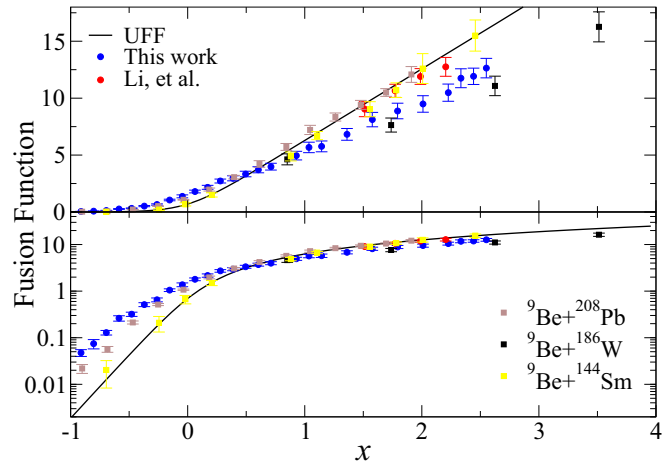

FIG. 13. Comparison between the UFF and renormalized fusion function for total fusion (TF). The systems are composed by the ^{9}Be projectile on different targets: ^{186}W [88], ^{144}Sm [89], ^{208}Pb [13], ^{197}Au from Ref. [42] and this work.

As one can see from Fig. 13, the TF for the ^{9}Be + ^{208}Pb, ^{144}Sm systems show no effect at energies above the barrier. The TF for the ^{9}Be + ^{197}Au system was measured by Ref. [42] and in the present work. While their data show no effect of the breakup + transfer channels on the TF above the Coulomb barrier, our reduced TF presents a hindrance of about 10%. The reduced TF for the ^{9}Be + ^{186}W shows a hindrance larger than 10%. These results show the necessity of more experimental data to elucidate the contradiction among different data sets reported in the literature. Below the Coulomb barrier, all the systems show an enhancement of the TF.

IV. DISCUSSION AND CONCLUSIONS

In the present work we measured the most important reaction channels that contribute to complete fusion, incomplete fusion and neutron transfer for the ^{9}Be + ^{197}Au system for a very extended range of energies around the Coulomb barrier. The offline method for the γ-ray detection of the β/ϵ decay products of the evaporation residues allowed us to measure all relevant neutron evaporation channels (more than 95% of the yield).

The elastic- and inelastic-scattering angular distributions of Ref. [46] at energies around the Coulomb barrier were reanalyzed using a double-folding parameter-free SPP. A very good description of both angular distributions was achieved. In the inelastic scattering, it was shown that the sum of two states (at 270 and 279 keV) was essential to describe the angular distributions experimentally not resolved.

Besides the inelastic scattering, the more relevant nonelastic reaction mechanisms were studied in detail: the one-neutron transfer channels (stripping and pickup), and fusion. Although the breakup of ^{9}Be was not measured, its effect of other reaction mechanisms was studied.

The CRC method was used to study the ^{197}Au(^{9}Be, ^{8}Be)^{198}Au striping reaction. At energies near and above the Coulomb barrier, the agreement with the experimental data can be achieved by including many states of the residual ^{198}Au nucleus. The coupling of the 2^{+} resonant state of ^{8}Be ejectile was of utmost relevance to describe the present experimental data, consistently with NCBU experiments with ^{9}Be projectiles [19]. At energies well below the barrier, the experimental data were underestimated. The neutron absorption after the breakup of the ^{9}Be projectile and the direct one-neutron stripping produces the same residual nucleus ^{198}Au. CDCC calculations were performed, and it was shown that, at energies below the Coulomb barrier, the elastic breakup is the dominant reaction mechanism. This might suggest that the target could absorb part of the neutrons produced from the breakup.

The CDCC calculations performed in this work were simplified. We only considered the breakup of the ^{9}Be into a neutron and ^{8}Be (that breaks into two alpha particles). This should be a more probable breakup channel of the projectile than its breakup into ^{5}He + ^{4}He because the last mechanism has a higher breakup threshold. Also, instead of performing four-body CDCC calculations, we performed three-body CDCC calculations. Four-body CDCC calculations for the ^{9}Be + ^{120}Sn [90] and ^{9}Be + ^{208}Pb [91] systems were recently performed. The effect of the breakup channel on the elastic-scattering angular distribution was also found small and slightly damping the Fresnel peak. Nevertheless, as the effect of the breakup on the other reaction mechanisms was found very weak, we believe that this is enough for the present work. The dynamic polarization potential found from our calculations had a repulsive real part at distances near the Coulomb barrier and an attractive imaginary part in the whole energy interval studied in the present work.

Concerning the one-neutron pickup reaction ^{197}Au(^{9}Be, ^{10}Be)^{196}Au, we obtained a fairly good description of the experimental data. The use of a standard value of 1.0 for the spectroscopic amplitudes of the ^{197}Au-^{198}Au overlaps might have produced a slight overestimation compared with the experimental data. The effect of the breakup mechanism on this channel was also found negligible.

To study the effect of the breakup plus transfer channels on the TF and CF, the UFF method proposed in Refs. [44,45] was used. For energies above the Coulomb barrier, the CF was hindered by about 45% compared with the benchmark universal fusion function. This is slightly above the 30%–35% systematic value obtained in Refs. [44,45], but in agreement with the value obtained for the same system by other groups [42,43,88]. At energies below the barrier, the CF was enhanced in agreement with the results reported in the literature. Concerning the TF, a hindrance of about 10% at energies above the Coulomb barrier was obtained. This result disagrees with the results found for the same system by Li *et al.* [42] and also with the results for the ^{9}Be + ^{208}Pb system [13]. By comparing our experimental data with those of Li *et al.*, one realizes that the only channel that does not agree is the $(\alpha, 2n)$ channel for the ICF. We did not find any reason for this disagreement. A systematic error should be disregarded, because this difference does not appear in other channels. Nevertheless, the TF hindrance observed in our work agrees with the results of Ref. [88]. Contradictions of this kind are also present for other systems of reactions induced by ^{9}Be [92] and deserve additional experimental studies. The TF below the barrier shows the typical enhancement common to the other studied systems.

ACKNOWLEDGMENTS

Argentinean authors acknowledge financial support from CONICET (Consejo Nacional de Investigaciones Científicas y Técnicas) through Grants No. PIP00786CO, No. PIP00625, and from FONCyT (Fondo para la Investigación Científica y Tecnológica) through Grant No. PICT-2017-4088. The Brazilian authors acknowledge financial support from the CNPq, FAPERJ, and INCT-FNA (Instituto Nacional de Ciência e Tecnologia-Física Nuclear e Aplicações) Proc. No. 464898/2014-5.

[1] L. Canto, P. Gomes, R. Donangelo, J. Lubian, and M. Hussein, Phys. Rep. **596**, 1 (2015).

[2] N. Keeley, R. Raabe, N. Alamanos, and J. Sida, Prog. Part. Nucl. Phys. **59**, 579 (2007).

[3] D. Savran, T. Aumann, and A. Zilges, Prog. Part. Nucl. Phys. **70**, 210 (2013).

[4] J. S. Wang, Y. Y. Yang, Q. Wang, L. Jin, J. B. Ma, M. R. Huang, J. L. Han, P. Ma, S. L. Jin, Z. Bai, Q. Hu, J. B. Chen, R. Wada, Z. Y. Sun, R. F. Chen, X. Y. Zhang, Z. G. Hu, X. H. Yuan, X. G. Cao, Z. G. Xu, S. W. Xu, C. Zhen, Z. Q. Chen, Z. Chen, S. Z. Chen, C. M. Du, L. M. Duan, F. Fu, B. X. Gou, J. Hu, J. J. He, X. G. Lei, S. L. Li, Y. Li, Q. Y. Lin, L. X. Liu, F. D. Shi, S. W. Tang, G. Xu, L. Y. Zhang, X. H. Zhang, W. Zhang, M. H. Zhao, Y. H. Zhang, H. S. Xu, G. Q. Xiao, S. Mukhejee, N. Keeley, K. Rusek, and D. Y. Pang, J. Phys.: Conf. Ser. **420**, 012075 (2013).

[5] I. J. Thompson and F. M. Nunes, *Nuclear Reactions for Astrophysics* (Cambridge University Press, Cambridge, 2009).

[6] A. Pakou, K. Rusek, N. Alamanos, X. Aslanoglou, S. Harissopulos, M. Kokkoris, A. Lagoyannis, T. J. Mertzimekis, A. Musumarra, N. G. Nicolis, C. Papachristodoulou, D. Pierroutsakou, and D. Roubos, Phys. Rev. C **76**, 054601 (2007).

[7] D. Heimann, A. Pacheco, O. Capurro, A. Arazi, P. Carnelli, M. Cardona, E. Barbará, J. Niello, J. Figueira, L. Fimiani, D. Hojman, G. Marti, and A. Negri, in *IX Latin American Symposium on Nuclear Physics and Applications*, edited by R. Alarcon, E. Ayala, C. Granja, and N. Medina, AIP Conf. Proc. No. 1423 (AIP, New York, 2012), p. 109.

[8] K. J. Cook, E. C. Simpson, D. H. Luong, S. Kalkal, M. Dasgupta, and D. J. Hinde, Phys. Rev. C **93**, 064604 (2016).

[9] M. A. G. Alvarez, J. P. Fernández-García, J. L. León-García, M. Rodríguez-Gallardo, L. R. Gasques, L. C. Chamon, V. A. B. Zagatto, A. Lépine-Szily, J. R. B. Oliveira, V. Scarduelli, B. V. Carlson, J. Casal, A. Arazi, D. A. Torres, and F. Ramirez, Phys. Rev. C **100**, 064602 (2019).

[10] C. H. Dasso and A. Vitturi, Phys. Rev. C **50**, R12 (1994).

[11] M. Dasgupta, D. J. Hinde, R. D. Butt, R. M. Anjos, A. C. Berriman, N. Carlin, P. R. S. Gomes, C. R. Morton, J. O. Newton, A. Szanto de Toledo, and K. Hagino, Phys. Rev. Lett. **82**, 1395 (1999).

[12] D. J. Hinde, M. Dasgupta, B. R. Fulton, C. R. Morton, R. J. Wooliscroft, A. C. Berriman, and K. Hagino, Phys. Rev. Lett. **89**, 272701 (2002).

[13] M. Dasgupta, P. R. S. Gomes, D. J. Hinde, S. B. Moraes, R. M. Anjos, A. C. Berriman, R. D. Butt, N. Carlin, J. Lubian, C. R. Morton, J. O. Newton, and A. Szanto de Toledo, Phys. Rev. C **70**, 024606 (2004).

[14] P. R. S. Gomes, I. Padron, E. Crema, O. A. Capurro, J. O. Fernández Niello, A. Arazi, G. V. Martí, J. Lubian, M. Trotta, A. J. Pacheco, J. E. Testoni, M. D. Rodríguez, M. E. Ortega, L. C. Chamon, R. M. Anjos, R. Veiga, M. Dasgupta, D. J. Hinde, and K. Hagino, Phys. Rev. C **73**, 064606 (2006).

[15] A. Mukherjee, Subinit Roy, M. Pradhan, M. Saha Sarkar, P. Basu, B. Dasmahapatra, T. Bhattacharya, S. Bhattacharya, S. Basu, A. Chatterjee, V. Tripathi, and S. Kailas, Phys. Lett. B **636**, 91 (2006).

[16] L. R. Gasques, D. J. Hinde, M. Dasgupta, A. Mukherjee, and R. G. Thomas, Phys. Rev. C **79**, 034605 (2009).

[17] E. F. Aguilera, E. Martinez-Quiroz, P. Rosales, J. J. Kolata, P. A. DeYoung, G. F. Peaslee, P. Mears, C. Guess, F. D. Becchetti, J. H. Lupton, and Y. Chen, Phys. Rev. C **80**, 044605 (2009).

[18] V. V. Parkar, R. Palit, S. K. Sharma, B. S. Naidu, S. Santra, P. K. Joshi, P. K. Rath, K. Mahata, K. Ramachandran, T. Trivedi, and A. Raghav, Phys. Rev. C **82**, 054601 (2010).

[19] R. Rafiei, R. du Rietz, D. H. Luong, D. J. Hinde, M. Dasgupta, M. Evers, and A. Diaz-Torres, Phys. Rev. C **81**, 024601 (2010).

[20] D. J. Hinde and M. Dasgupta, Phys. Rev. C **81**, 064611 (2010).

[21] P. Gomes, L. Canto, J. Lubian, and M. Hussein, Phys. Lett. B **695**, 320 (2011).

[22] P. R. S. Gomes, D. R. Otomar, T. Correa, L. F. Canto, J. Lubian, R. Linares, D. H. Luong, M. Dasgupta, D. J. Hinde, and M. S. Hussein, J. Phys. G **39**, 115103 (2012).

[23] D. Luong, M. Dasgupta, D. Hinde, R. du Rietz, R. Rafiei, C. Lin, M. Evers, and A. Diaz-Torres, Phys. Lett. B **695**, 105 (2011).

[24] N. T. Zhang, Y. D. Fang, P. R. S. Gomes, J. Lubian, M. L. Liu, X. H. Zhou, G. S. Li, J. G. Wang, S. Guo, Y. H. Qiang, Y. H. Zhang, D. R. Mendes Junior, Y. Zheng, X. G. Lei, B. S. Gao, Z. G. Wang, K. L. Wang, and X. F. He, Phys. Rev. C **90**, 024621 (2014).

[25] Y. D. Fang, P. R. S. Gomes, J. Lubian, M. L. Liu, X. H. Zhou, D. R. Mendes Junior, N. T. Zhang, Y. H. Zhang, G. S. Li, J. G. Wang, S. Guo, Y. H. Qiang, B. S. Gao, Y. Zheng, X. G. Lei, and Z. G. Wang, Phys. Rev. C **91**, 014608 (2015).

[26] D. H. Luong, M. Dasgupta, D. J. Hinde, R. du Rietz, R. Rafiei, C. J. Lin, M. Evers, and A. Diaz-Torres, Phys. Rev. C **88**, 034609 (2013).

[27] K. J. Cook, E. C. Simpson, L. T. Bezzina, M. Dasgupta, D. J. Hinde, K. Banerjee, A. C. Berriman, and C. Sengupta, Phys. Rev. Lett. **122**, 102501 (2019).

[28] J. Rangel, M. Cortes, J. Lubian, and L. Canto, Phys. Lett. B **803**, 135337 (2020).

[29] M. R. Cortes, J. Rangel, J. L. Ferreira, J. Lubian, and L. F. Canto, Phys. Rev. C **102**, 064628 (2020).

[30] B. R. Fulton, R. L. Cowin, R. J. Woolliscroft, N. M. Clarke, L. Donadille, M. Freer, P. J. Leask, S. M. Singer, M. P. Nicoli, B. Benoit, F. Hanappe, A. Ninane, N. A. Orr, J. Tillier, and L. Stuttgé, Phys. Rev. C **70**, 047602 (2004).

[31] N. I. Ashwood, M. Freer, D. J. Millener, N. A. Orr, F. Carstoiu, S. Ahmed, J. C. Angélique, V. Bouchat, W. N. Catford, N. M. Clarke, N. Curtis, F. Hanappe, M. Horoi, Y. Kerckx, J. L. Lecouey, F. M. Marqués, T. Materna, G. Normand, S. Pain, N. Soić *et al.*, Phys. Rev. C **72**, 024314 (2005).

[32] P. Papka, T. A. D. Brown, B. R. Fulton, D. L. Watson, S. P. Fox, D. Groombridge, M. Freer, N. M. Clarke, N. I. Ashwood, N. Curtis, V. Ziman, P. McEwan, S. Ahmed, W. N. Catford, D. Mahboub, C. N. Timis, T. D. Baldwin, and D. C. Weisser, Phys. Rev. C **75**, 045803 (2007).

[33] T. A. D. Brown, P. Papka, B. R. Fulton, D. L. Watson, S. P. Fox, D. Groombridge, M. Freer, N. M. Clarke, N. I. Ashwood, N. Curtis, V. Ziman, P. McEwan, S. Ahmed, W. N. Catford, D. Mahboub, C. N. Timis, T. D. Baldwin, and D. C. Weisser, Phys. Rev. C **76**, 054605 (2007).

[34] R. Anjos, C. Muri, J. Lubian, P. Gomes, I. Padron, J. Alves, G. Martí, J. Fernández Niello, A. Pacheco, O. Capurro, D. Abriola, J. Testoni, M. Ramírez, R. Liguori Neto, and N. Added, Phys. Lett. B **534**, 45 (2002).

[35] S. B. Moraes, P. R. S. Gomes, J. Lubian, J. J. S. Alves, R. M. Anjos, M. M. Sant'Anna, I. Padrón, C. Muri, R. Liguori Neto, and N. Added, Phys. Rev. C **61**, 064608 (2000).

[36] P. Gomes, I. Padron, M. Rodríguez, G. Martí, R. Anjos, J. Lubian, R. Veiga, R. Liguori Neto, E. Crema, N. Added, L. Chamon, J. Fernández Niello, O. Capurro, A. Pacheco, J. Testoni, D. Abriola, A. Arazi, M. Ramírez, and M. Hussein, Phys. Lett. B **601**, 20 (2004).

[37] P. R. S. Gomes, M. D. Rodríguez, G. V. Martí, I. Padron, L. C. Chamon, J. O. Fernández Niello, O. A. Capurro, A. J. Pacheco,

J. E. Testoni, A. Arazi, M. Ramírez, R. M. Anjos, J. Lubian, R. Veiga, R. Liguori Neto, E. Crema, N. Added, C. Tenreiro, and M. S. Hussein, Phys. Rev. C **71**, 034608 (2005).
[38] R. J. Woolliscroft, N. M. Clarke, B. R. Fulton, R. L. Cowin, M. Dasgupta, D. J. Hinde, C. R. Morton, and A. C. Berriman, Phys. Rev. C **68**, 014611 (2003).
[39] M. Dasgupta, D. J. Hinde, S. L. Sheehy, and B. Bouriquet, Phys. Rev. C **81**, 024608 (2010).
[40] C. Signorini, Z. H. Liu, Z. C. Li, K. E. G. Löbner, L. Müller, M. Ruan, K. Rudolph, F. Soramel, C. Zotti, A. Andrighetto, L. Stroe, A. Vitturi, and H. Q. Zhang, Eur. Phys. J. A **5**, 7 (1999).
[41] R. Raabe, C. Angulo, J. L. Charvet, C. Jouanne, L. Nalpas, P. Figuera, D. Pierroutsakou, M. Romoli, and J. L. Sida, Phys. Rev. C **74**, 044606 (2006).
[42] G. S. Li, J. G. Wang, J. Lubian, H. O. Soler, Y. D. Fang, M. L. Liu, N. T. Zhang, X. H. Zhou, Y. H. Zhang, B. S. Gao, Y. H. Qiang, S. Guo, S. C. Wang, K. L. Wang, K. K. Zheng, R. Li, and Y. Zheng, Phys. Rev. C **100**, 054601 (2019).
[43] M. Kaushik, G. Gupta, S. Thakur, H. Krishnamoorthy, P. P. Singh, V. V. Parkar, V. Nanal, A. Shrivastava, R. G. Pillay, K. Mahata, K. Ramachandran, S. Pal, C. S. Palshetkar, and S. K. Pandit, Phys. Rev. C **101**, 034611 (2020).
[44] L. Canto, P. Gomes, J. Lubian, L. Chamon, and E. Crema, J. Phys. G **36**, 015109 (2008).
[45] L. Canto, P. Gomes, J. Lubian, L. Chamon, and E. Crema, Nucl. Phys. A **821**, 51 (2009).
[46] F. Gollan, D. Abriola, A. Arazi, M. Cardona, E. de Barbará, D. Hojman, R. Id Betan, G. Martí, A. Pacheco, D. Rodrigues, and M. Togneri, Nucl. Phys. A **1000**, 121789 (2020).
[47] J. Wilczyński and K. Siwek-Wilczynska, Phys. Lett. B **55**, 270 (1975).
[48] J. F. Ziegler, M. Ziegler, and J. Biersack, Nucl. Instrum. Methods Phys. Res. Sect. B **268**, 1818 (2010).
[49] M. Aversa, D. Abriola, M. A. G. Alvarez, A. Arazi, M. A. Cardona, L. C. Chamon, E. de Barbará, J. de Jesús, J. P. Fernández-García, L. R. Gasques, D. Hojman, A. Lépine-Szily, G. V. Martí, A. J. Pacheco, V. Scarduelli, and V. A. B. Zagatto, Phys. Rev. C **101**, 044601 (2020).
[50] A. Gavron, Phys. Rev. C **21**, 230 (1980).
[51] F. Kondev, Nucl. Data Sheets **105**, 1 (2005).
[52] S. Zhu and F. Kondev, Nucl. Data Sheets **109**, 699 (2008).
[53] F. Kondev, Nucl. Data Sheets **108**, 365 (2007).
[54] F. Kondev and S. Lalkovski, Nucl. Data Sheets **108**, 1471 (2007).
[55] B. Singh, Nucl. Data Sheets **108**, 79 (2007).
[56] X. Huang and M. Kang, Nucl. Data Sheets **133**, 221 (2016).
[57] H. Xiaolong, Nucl. Data Sheets **108**, 1093 (2007).
[58] M. Wang, G. Audi, F. G. Kondev, W. Huang, S. Naimi, and X. Xu, Chin. Phys. C **41**, 030003 (2017).
[59] R. Firestone, Nucl. Data Sheets **108**, 2319 (2007).
[60] J. Chen, Nucl. Data Sheets **140**, 1 (2017).
[61] See Supplemental Material at http://link.aps.org/supplemental/10.1103/PhysRevC.104.024609 for full table of the experimental n transfer and complete and incomplete fusion cross sections.
[62] L. C. Chamon, D. Pereira, M. S. Hussein, M. A. Cândido Ribeiro, and D. Galetti, Phys. Rev. Lett. **79**, 5218 (1997).
[63] D. Pereira, J. Lubian, J. R. B. Oliveira, D. P. de Sousa, and L. C. Chamon, Phys. Lett. B **670**, 330 (2009).
[64] E. Barnard, J. De Villiers, C. Engelbrecht, and D. Reitmann, Nucl. Phys. A **167**, 511 (1971).
[65] I. J. Thompson, Comput. Phys. Rep. **7**, 167 (1988).
[66] L. R. Gasques, L. C. Chamon, P. R. S. Gomes, and J. Lubian, Nucl. Phys. A **764**, 135 (2006).
[67] M. Cavallaro, F. Cappuzzello, M. Bondì, D. Carbone, V. N. Garcia, A. Gargano, S. M. Lenzi, J. Lubian, C. Agodi, F. Azaiez, M. De Napoli, A. Foti, S. Franchoo, R. Linares, D. Nicolosi, M. Niikura, J. A. Scarpaci, and S. Tropea, Phys. Rev. C **88**, 054601 (2013).
[68] M. J. Ermamatov, F. Cappuzzello, J. Lubian, M. Cubero, C. Agodi, D. Carbone, M. Cavallaro, J. L. Ferreira, A. Foti, V. N. Garcia, A. Gargano, J. A. Lay, S. M. Lenzi, R. Linares, G. Santagati, and A. Vitturi, Phys. Rev. C **94**, 024610 (2016).
[69] D. Carbone, J. L. Ferreira, F. Cappuzzello, J. Lubian, C. Agodi, M. Cavallaro, A. Foti, A. Gargano, S. M. Lenzi, R. Linares, and G. Santagati, Phys. Rev. C **95**, 034603 (2017).
[70] M. J. Ermamatov, R. Linares, J. Lubian, J. L. Ferreira, F. Cappuzzello, D. Carbone, M. Cavallaro, M. Cubero, P. N. de Faria, A. Foti, G. Santagati, and V. A. B. Zagatto, Phys. Rev. C **96**, 044603 (2017).
[71] V. Scarduelli, E. Crema, V. Guimarães, D. Abriola, A. Arazi, E. de Barbará, O. A. Capurro, M. A. Cardona, J. Gallardo, D. Hojman, G. V. Martí, A. J. Pacheco, D. Rodrígues, Y. Y. Yang, N. N. Deshmukh, B. Paes, J. Lubian, D. R. Mendes Junior, V. Morcelle, and D. S. Monteiro, Phys. Rev. C **96**, 054610 (2017).
[72] B. Paes, G. Santagati, R. M. Vsevolodovna, F. Cappuzzello, D. Carbone, E. N. Cardozo, M. Cavallaro, H. García-Tecocoatzi, A. Gargano, J. L. Ferreira, S. M. Lenzi, R. Linares, E. Santopinto, A. Vitturi, and J. Lubian, Phys. Rev. C **96**, 044612 (2017).
[73] R. Linares, M. J. Ermamatov, J. Lubian, F. Cappuzzello, D. Carbone, E. N. Cardozo, M. Cavallaro, J. L. Ferreira, A. Foti, A. Gargano, B. Paes, G. Santagati, and V. A. B. Zagatto, Phys. Rev. C **98**, 054615 (2018).
[74] G. L. Zhang, G. X. Zhang, S. P. Hu, Y. J. Yao, J. B. Xiang, H. Q. Zhang, J. Lubian, J. L. Ferreira, B. Paes, E. N. Cardozo, H. B. Sun, J. J. Valiente-Dobón, D. Testov, A. Goasduff, P. R. John, M. Siciliano, F. Galtarossa, R. Francesco, D. Mengoni, D. Bazzacco *et al.*, Phys. Rev. C **97**, 014611 (2018).
[75] E. Crema, V. A. B. Zagatto, J. M. B. Shorto, B. Paes, J. Lubian, R. F. Simões, D. S. Monteiro, J. F. P. Huiza, N. Added, M. C. Morais, and P. R. S. Gomes, Phys. Rev. C **98**, 044614 (2018).
[76] E. Crema, V. A. B. Zagatto, J. M. B. Shorto, B. Paes, J. Lubian, R. F. Simões, D. S. Monteiro, J. F. P. Huiza, N. Added, M. C. Morais, and P. R. S. Gomes, Phys. Rev. C **99**, 054623 (2019).
[77] U. Umbelino, K. C. C. Pires, R. Lichtenthäler, V. Scarduelli, G. A. Scotton, A. Lépine-Szily, V. Guimarães, J. Lubian, B. Paes, J. L. Ferreira, M. A. G. Alvarez, J. M. B. Shorto, S. Appannababu, M. Assunç ao, R. P. Condori, and V. Morcelle, Phys. Rev. C **99**, 064617 (2019).
[78] V. A. B. Zagatto, E. Crema, J. M. B. Shorto, M. C. Morais, J. Lubian, N. Added, R. F. Simões, D. S. Monteiro, J. F. P. Huiza, B. Paes, and P. R. S. Gomes, Phys. Rev. C **100**, 044602 (2019).
[79] E. Crema, B. Paes, V. A. B. Zagatto, J. F. P. Huiza, J. Lubian, J. M. B. Shorto, R. F. Simões, D. S. Monteiro, N. Added, M. C. Morais, and P. R. S. Gomes, Phys. Rev. C **100**, 054608 (2019).
[80] E. N. Cardozo, M. J. Ermamatov, J. L. Ferreira, B. Paes, M. Sinha, and J. Lubian, Eur. Phys. J. A **54**, 150 (2018).
[81] A. Koning and J. Delaroche, Nucl. Phys. A **713**, 231 (2003).
[82] J. Lang, R. Müller, J. Unternährer, L. Jarczyk, B. Kamys, and A. Strzalkowski, Phys. Rev. C **16**, 1448 (1977).

[83] L. F. Canto, R. Donangelo, M. S. Hussein, P. Lotti, J. Lubian, and J. Rangel, Phys. Rev. C **98**, 044617 (2018).
[84] NuShellX for Windows and Linux http://www.garsington.eclipse.co.uk/.
[85] Y. Utsuno and S. Chiba, Phys. Rev. C **83**, 021301(R) (2011).
[86] E. Warburton, B. Brown, and D. Millener, Phys. Lett. B **293**, 7 (1992).
[87] C. Wong, Phys. Rev. Lett. **31**, 766 (1973).
[88] Y. D. Fang, P. R. S. Gomes, J. Lubian, X. H. Zhou, Y. H. Zhang, J. L. Han, M. L. Liu, Y. Zheng, S. Guo, J. G. Wang, Y. H. Qiang, Z. G. Wang, X. G. Wu, C. Y. He, Y. Zheng, C. B. Li, S. P. Hu, and S. H. Yao, Phys. Rev. C **87**, 024604 (2013).
[89] P. Gomes, J. Lubian, B. Paes, V. Garcia, D. Monteiro, I. Padrón, J. Figueira, A. Arazi, O. Capurro, L. Fimiani, A. Negri, G. Martí, J. F. Niello, A. Gómez-Camacho, and L. Canto, Nucl. Phys. A **828**, 233 (2009).
[90] A. Arazi, J. Casal, M. Rodríguez-Gallardo, J. M. Arias, R. Lichtenthaler Filho, D. Abriola, O. A. Capurro, M. A. Cardona, P. F. F. Carnelli, E. de Barbará, J. Fernandez Niello, J. M. Figueira, L. Fimiani, D. Hojman, G. V. Martí, D. Martinez Heimman, and A. J. Pacheco, Phys. Rev. C **97**, 044609 (2018).
[91] J. Casal, M. Rodríguez-Gallardo, and J. M. Arias, Phys. Rev. C **92**, 054611 (2015).
[92] P. R. S. Gomes, R. Linares, J. Lubian, C. C. Lopes, E. N. Cardozo, B. H. F. Pereira, and I. Padron, Phys. Rev. C **84**, 014615 (2011).